

Anisotropy of Density Fluctuations in the Solar Wind at 1 au

JIAMING WANG,¹ ROHIT CHHIBER,^{1,2} SOHOM ROY,¹ MANUEL E. CUESTA,³ FRANCESCO PECORA,¹ YAN YANG,¹
XIANGRONG FU,^{4,5} HUI LI,⁵ AND WILLIAM H. MATTHAEUS¹

¹*Department of Physics and Astronomy, University of Delaware*

²*Heliophysics Science Division, NASA Goddard Space Flight Center*

³*Department of Astrophysical Sciences, Princeton University*

⁴*New Mexico Consortium, Los Alamos, NM 87544*

⁵*Los Alamos National Laboratory, Los Alamos, NM 87545*

(Dated: February 9, 2024)

ABSTRACT

A well-known property of solar wind plasma turbulence is the observed anisotropy of the autocorrelations, or equivalently the spectra, of velocity and magnetic field fluctuations. Here we explore the related but apparently not well-studied issue of the anisotropy of plasma density fluctuations in the energy-containing and inertial ranges of solar wind turbulence. Using 10 years (1998-2008) of *in situ* data from the Advanced Composition Explorer (ACE) mission, we find that the density correlation scale is slightly larger in directions quasi-parallel to the large-scale mean magnetic field as compared to quasi-perpendicular directions. The effect is present in both fast and slow winds. The anisotropy as a function of the level of correlation is also explored. We find at small correlation levels, i.e., at energy-containing scales and larger, the density fluctuations are close to isotropy, but in fact slightly favor more rapid decorrelation in perpendicular directions. At relatively smaller turbulence inertial range scales where the correlation values are larger, the sense of anisotropy is reversed in all speed ranges, implying a more “slab-like” structure, especially prominent in the fast wind samples. We contrast this finding with published results on velocity and magnetic field correlations.

1. INTRODUCTION

There are two well-known reasons for turbulent fluctuations in the solar wind to exhibit departures from statistical isotropy (Batchelor 1970; Oughton et al. 2015). The first is solar wind expansion, which in the simplest terms imposes the radial coordinate as a preferred direction. This is expected to influence mainly those structures larger than the turbulence correlation scales. For smaller-scale structures, including the inertial and kinetic ranges, the second influence - that of the

local large-scale magnetic field - is expected to exert a dominant influence. Indeed, it is well established that in the inertial range of magnetohydrodynamic (MHD) turbulence, the correlation functions (or equivalently, the spectra) of magnetic field and velocity fluctuations exhibit anisotropy relative to the magnetic field direction (Matthaeus et al. 1990, 1996; Chen et al. 2012; Shaikh & Zank 2010; Oughton et al. 2015). The symmetries that may be associated with this anisotropy may be referred to as rotational symmetries, such as axisymmetric “slab” or “2D” geometries (Bieber

et al. 1996). The analogous issue of anisotropy of density fluctuations has received some attention, reviewed below, in the theoretical and numerical simulation literature (Matthaeus et al. 1996; Cho & Lazarian 2002; Chandran & Backer 2002; Zank et al. 2012) as well as in remote sensing observations (Coles & Harmon 1989). However, to our knowledge, the issue of correlation or spectral anisotropy of the density fluctuation field in the energy-containing and inertial ranges of turbulence has not been fully examined in solar wind *in situ* observations. Here we take a step in that direction by examining density correlation statistics, their variation relative to the mean magnetic field and their variation with scale. (Mean values and other statistics are computed over samples of at least a correlation scale, in accord with classical ergodic theory; see e.g., Panchev (1971).) As in the usual picture of turbulence, scales can be categorized as the energy-containing, inertial, and dissipation regimes. Here, we focus on the former two, which are roughly separated by the correlation scale (Frisch 1995). Our study emphasizes observations near 1 au, where long-term datasets provide the possibility of high statistical weight analyses.

Coronal and solar wind density fluctuations can be studied based on remote sensing techniques, such as analysis of scintillation of signals from distant radio sources (Coles & Harmon 1989; Armstrong et al. 1990; Kellogg & Horbury 2005; Kontar et al. 2023). Rotational symmetry is frequently extracted from these measurements. Many of these studies are designed to detect coronal density properties, while a few have been carried out near 1 au. The seminal work of Celnikier et al. (1987) describes the limitations and sensitivities of this class of scintillation studies. A typical conclusion is that structures in the coronal density fluctuation field are preferentially elongated in the direction of the inferred mean magnetic field. This implies that density gradients are stronger in directions perpendicular to the magnetic field. This sense of correlation anisotropy is familiar in solar

wind measurements of velocity and magnetic field (Matthaeus et al. 1990; Bieber et al. 1996; Hamilton et al. 2008; Narita et al. 2010; Chen et al. 2011; Horbury et al. 2012; Oughton et al. 2015).

Interplanetary density spectra have also been examined based on *in situ* observations (see, e.g. Bellamy et al. 2005). But the directional dependence of density fluctuation statistics in the inertial and energy-containing ranges of scales have sometimes been overlooked, even in relatively complete characterizations of turbulence correlations (Borovsky 2012). When density fluctuations have been considered, the emphasis has often been on high frequency or sub-ion scales (Celnikier et al. 1987; Malaspina et al. 2010; Chen et al. 2011; Kontar et al. 2023) where kinetic plasma properties are probed. However, we are not aware that a comprehensive survey has been carried out to describe the anisotropy of MHD-scale inertial-range correlation of the plasma density. This motivates our current focus on the anisotropy of energy-containing range and inertial range density fluctuations near Earth’s orbit.

This paper is organized as follows: in Section 2 we discuss the “Maltese cross” representation of correlation anisotropy, which serves as the theoretical basis prompting this research. In Section 3 we describe our data and analysis procedure. Section 4 presents our results on the scale-dependent density correlation anisotropy, and Section 5 discusses the implications of the results.

2. SIMPLIFIED REPRESENTATIONS OF ANISOTROPY

A point of reference that motivates the present study is the “Maltese cross” autocorrelation pattern (Matthaeus et al. 1990) derived from the interplanetary magnetic field (IMF) at 1 au. The pattern is assumed to be axisymmetric about the mean magnetic field \mathbf{B}_0 and consists of a lobe that admits gradients mainly in the direction parallel to \mathbf{B}_0 and another part that varies mainly in the

directions perpendicular to \mathbf{B}_0 . In an idealized sense, the former are known as “slab” fluctuations, and the latter, “2D” fluctuations. This so called *two-component model* has become a useful parameterization for anisotropy that incorporates both Alfvén wave-like spectral components and a quasi-two-dimensional (2D or Q2D) ingredient that varies, at most, weakly along a mean field (Bieber et al. 1994, 1996). The two-component parameterization allows for arbitrary admixtures of energy in models that vary mainly along or transverse to the mean field, and as such has become a convenient and often-invoked model for use in theoretical work on charged particle scattering (Shalchi 2009). It is also incorporated with several variations into turbulence transport models that describe turbulence throughout the heliosphere as well as models for solar wind acceleration and evolution in the presence of turbulence (e.g., Adhikari et al. 2017; Usmanov et al. 2018). The anisotropy present in such models exerts a strong influence on the results of such calculations and modeling of turbulence. It is essential to bear in mind that such parameterization of anisotropy are crude representations, and are not intended as dynamical turbulence models. However, they demonstrate the physical significance and impact of correlation or spectral anisotropy.

Another approach to describing spectral anisotropy is based on wave theory, with the premise being that linear MHD wave modes may be separated unambiguously based on their polarization properties (Cho & Lazarian 2002; Cho et al. 2002). (The standard decomposition has been controversial for some time and recently a more complete approximate representation that includes structures as well as waves has been suggested by Zank et al. (2023).) This wave decomposition idea can be directly carried over to turbulence in the *weak turbulence* regime. In that case, the adopted basis and leading-order dynamical solutions are constructed from the linear modes themselves (Chandran 2005). In this view, the Alfvén mode is anisotropic, a well-established

property in strong MHD turbulence (Shebalin et al. 1983; Oughton et al. 1994). In addition, the Alfvén mode is polarized transverse to the mean magnetic field, a small-amplitude property adopted in *critical balance* theory by Goldreich & Sridhar (1995) (see also Oughton & Matthaeus 2020). The slow mode is assumed to follow a passive dynamics, and to admit an anisotropy similar to the incompressible Alfvén mode. The decomposition into wave modes is completed by extracting fluctuations with the polarization of linear fast modes. These remain isotropic, as the fast mode dispersion does not depend on direction. It is widely regarded that useful results have been attained based on a linear-wave decomposition. However, it should be disparaged as a general representation of MHD turbulence, as it has been shown to be essentially incomplete (Zank et al. 2023); in particular it lacks coherent structures and nonpropagating structures that are nonetheless found to be dynamically important (Gan et al. 2022).

The linear wave theory underlies a popular surrogate for compressional effects, the so-called *magnetic compressibility*, that has been extensively employed in observational solar wind studies (Bruno & Carbone 2013; Chen et al. 2012). This surrogate assumes that the relative strength of the component of the magnetic variance parallel to the ambient (mean) magnetic field is a measure of compressional dynamical activity. This assumption breaks down for large-amplitude turbulence, wherein parallel fluctuations need not be identified with compressional fast magnetosonic modes. Such fluctuations could have a more general character, such as an indication of spherical polarization of large-amplitude Alfvénic fluctuations (Barnes & Hollweg 1974; Barnes 1981), which are usually not associated with density variations.

In the following, we will not make explicit use of representations based on mode decomposition, but rather will incorporate the underlying ideas

Table 1. ACE 24-hour dataset count in each wind speed and angular channel. The angle θ is defined in Eq. 1

	≤ 400 km/s	400-500 km/s	≥ 500 km/s
0°-40°	68	89	56
40°-45°	95	130	124
45°-50°	214	343	348
50°-55°	370	541	620
55°-60°	469	672	524
60°-70°	754	714	331
70°-90°	196	132	50
Total	2166	2621	2053

into our physical discussion of the anisotropy of solar wind density fluctuations.

3. DATA AND ANALYSIS PROCEDURE

We acquire 10 years (from February 1998 to March 2008) of ion number density data observed by the SWEPAM instrument on the Advanced Composition Explorer (ACE) spacecraft (McComas et al. 1998), along with corresponding solar wind speed measurements from SWEPAM and magnetic field measurements from the MAG instrument (Smith et al. 1998) on ACE. This dataset covers most of a solar activity cycle, with maximum sunspot number occurring in 2003 (e.g., Balmeda et al. 2009). The original data at 64-second resolution is upsampled to a 1-minute cadence and separated into datasets that span one day. Overlapping midnight-to-midnight and noon-to-noon intervals are included to increase the total number of datasets and suppress systematic day-timescale periodicities. A density interval is discarded if over 70% of the observations are empty. In the retained intervals, any missing data is excluded from our computations. We then detrend each dataset using a linear fit, resulting in zero-mean data samples.

We group the data intervals based on their mean solar wind speed V_{SW} and the angle between

their mean magnetic field and the heliocentric radial direction:

$$\theta = \cos^{-1} \left(\frac{\mathbf{B}_0 \cdot \mathbf{r}}{|\mathbf{B}_0| |\mathbf{r}|} \right) \quad (1)$$

where \mathbf{r} is a vector in the radial direction and \mathbf{B}_0 is the mean magnetic field vector for a dataset. As the wind velocity is assumed to be radial, θ essentially represents the angle between the spacecraft sampling direction and the mean magnetic field. The θ channels are 0–40, 40–45, 45–50, 50–55, 55–60, 60–70, and 70–90 degrees, and the V_{SW} channels are 0–400, 400–500, and 500–1000 km/s for slow, medium, and fast winds, respectively. The channels are chosen to ensure a sufficient number of datasets in each group, as shown in Table 1 (also see the Appendix for a distribution of the solar wind speeds).

To proceed with our analysis, we compute the density autocorrelation function for each dataset using the Blackman-Tukey method (Blackman & Tukey 1958) (as described in detail in Roy et al. (2021)). The ensemble definition of the autocorrelation is

$$R(\tau) = \langle \rho(t)\rho(t+\tau) \rangle - \langle \rho(t) \rangle \langle \rho(t+\tau) \rangle \quad (2)$$

where ρ is the ion density, τ is the time lag. Invoking the ergodic theorem, the brackets $\langle \dots \rangle$ correspond formally to averaging over an infinite sample size. For finite data consisting of N equally spaced samples, we denote the averaging operation as $\langle \dots \rangle'$. Specifically, for a dataset $\{\rho_i\} = \rho_0, \dots, \rho_{N-1}$ with sampling time $\Delta t = 60$ seconds, τ takes integer multiples of Δt , and the averaging can be written explicitly as

$$\langle \rho(t) \rangle' = \langle \rho_j \rangle_{j=0, \dots, N-\tau/\Delta t-1}, \quad (3)$$

$$\langle \rho(t+\tau) \rangle' = \langle \rho_j \rangle_{j=\tau/\Delta t, \dots, N-1}, \quad (4)$$

$$\langle \rho(t)\rho(t+\tau) \rangle' = \langle \rho_j \rho_{j+\tau/\Delta t} \rangle_{j=0, \dots, N-\tau/\Delta t-1}. \quad (5)$$

For the remainder of the paper, for clarity, we drop the prime in the bracket notation.

For stationary data, $R(\tau)$ does not depend on the variable t , i.e. the origin of time. And

therefore by definition, the correlation function is an even function of lag τ . Under appropriate conditions, this is equivalent to the Reynolds averaging expression for the correlation function, $R(\tau) = \langle \delta\rho(t)\delta\rho(t+\tau) \rangle$, where $\delta\rho(t) \equiv \rho(t) - \langle \rho(t) \rangle$ (see Germano 1992).

When we consider the normalized correlation function \hat{R} , the $R(\tau)$ resulting from Eq. 2 is normalized by the data variance $R(0)$:

$$\hat{R}(\tau) = \frac{R(\tau)}{R(0)}. \quad (6)$$

To eliminate undersampled fluctuations at large lags, we pass each autocorrelation function through a 10% cosine taper window (Matthaeus & Goldstein 1982), where the last 10% of $\hat{R}(\tau)$ values are multiplied by the factor

$$\frac{1}{2} \left(1 + \cos \left[\frac{\pi}{0.1\tau_{\max}} (\tau - 0.9\tau_{\max}) \right] \right) \quad (7)$$

with τ_{\max} representing the maximum lag over which the autocorrelation is calculated. In this analysis the maximum lag is 4.8 hours; this corresponds to 1/5 of the data interval, and several times the anticipated correlation times.

We further transform the temporal lags τ into spatial lags λ by applying the Taylor frozen-in hypothesis (Taylor 1938), $\lambda = -V_{\text{SW}}\tau$, where V_{SW} is the solar wind speed in the upstream direction averaged over the data interval. With this procedure, we arrive at a normalized, spatial lag-dependent correlation function $\hat{R}(\lambda)$.

4. RESULTS

We first examine distributions of the standard deviations (S.D.; a measure of the fluctuation amplitude) of the density samples. The S.D. values range from 0.6 to 3.4 cm^{-3} across the 24-hour datasets, and increase with θ and decrease with V_{SW} . We plot in Fig. 1 the average sample S.D. with respect to θ and V_{SW} , with error bars representing standard errors. These plots indicate that

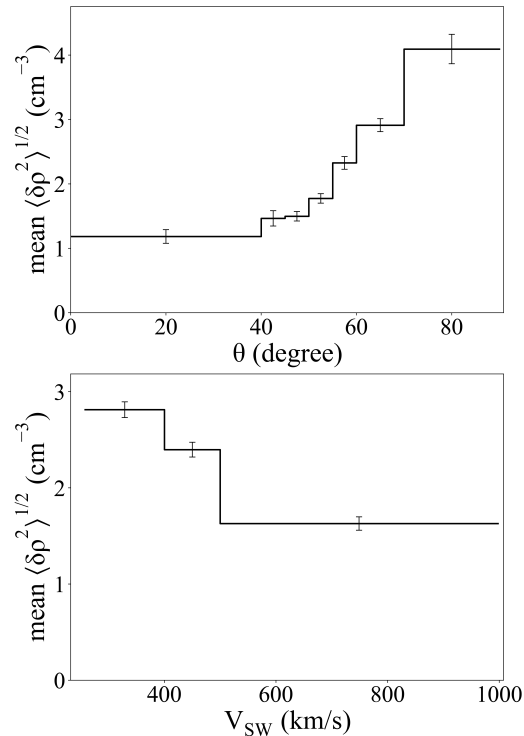


Figure 1. The density standard deviation averaged over each θ channel (top panel) and each V_{SW} channel (bottom panel). Error bars represent standard errors. Here $\delta\rho(t) \equiv \rho(t) - \langle \rho(t) \rangle$, where $\langle \dots \rangle$ refers to an average over an individual 24-hr dataset, and “mean” refers to averaging the standard deviations over all 24-hour datasets that lie within a θ or V_{SW} channel.

density fluctuations are stronger when the spacecraft samples flow perpendicular to, rather than parallel to, the mean magnetic field, and that slow wind exhibits larger density fluctuations compared to fast wind. (It is well-known that slow wind is denser than fast wind (McComas et al. 2000; Usmanov et al. 2018).) The top panel of Fig. 1 is consistent with the recent work of Du et al. (2023), on the anisotropy of density fluctuations obtained from simulations of compressible MHD turbulence.

We proceed to our investigation of the correlation anisotropy. The normalized autocorrelation functions are averaged within each group

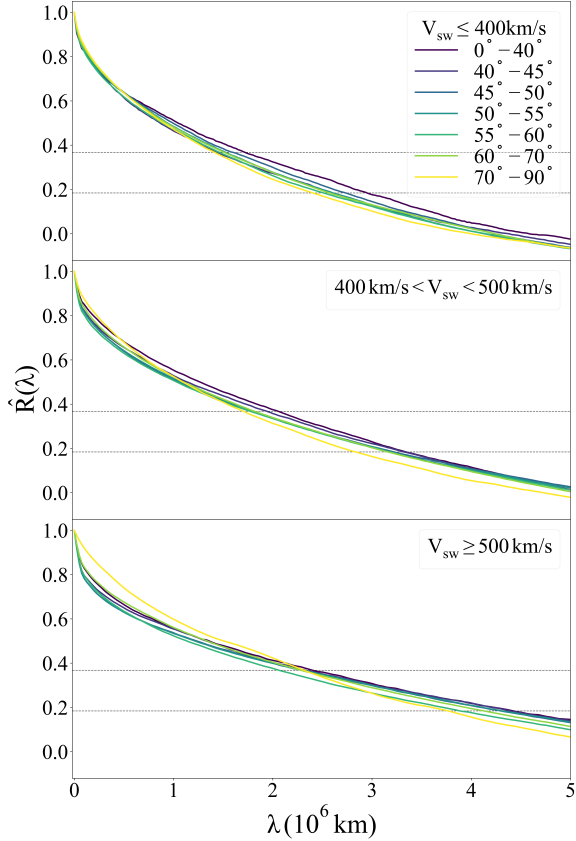


Figure 2. The normalized correlations for slow (top panel), medium (middle panel), and fast (bottom panel) winds as functions of spatial lag. The correlations have been averaged within each angular channel, denoted by distinctly colored lines. Dashed horizontal lines indicate where $\hat{R} = 1/e$ and $1/2e$.

of speed and angular channel, resulting in 21 instances of autocorrelations henceforth represented by $\hat{R}(\lambda = -V_{\text{SW}}\tau)$. These are shown in the panels of Fig. 2. Separate panels correspond to slow, medium, and fast winds, and within each, angular variations are demonstrated.

The correlation length λ_c , defined as the spatial lag where the correlation decreases by a factor of $1/e$, is listed in Table 2 for each channel. The uncertainties are standard errors calculated from the ensemble of intervals within each channel. We further plot λ_c over θ for all three wind channels

Table 2. Correlation length from the $1/e$ method and the length where correlation decreases by $1/2e$ (in parentheses) in units of 10^6 km in each wind speed and angular channel. The uncertainties represent standard errors.

	≤ 400 km/s	400-500 km/s	≥ 500 km/s
0°-40°	$1.73 \pm .16$ ($2.95 \pm .18$)	$2.08 \pm .13$ ($3.36 \pm .16$)	$2.40 \pm .24$ ($4.43 \pm .32$)
40°-45°	$1.45 \pm .13$ ($2.60 \pm .15$)	$1.95 \pm .11$ ($3.33 \pm .14$)	$2.33 \pm .16$ ($4.41 \pm .19$)
45°-50°	$1.60 \pm .09$ ($2.75 \pm .09$)	$1.83 \pm .07$ ($3.23 \pm .09$)	$2.30 \pm .10$ ($4.31 \pm .12$)
50°-55°	$1.53 \pm .07$ ($2.63 \pm .08$)	$1.80 \pm .06$ ($3.21 \pm .07$)	$2.33 \pm .07$ ($4.33 \pm .09$)
55°-60°	$1.48 \pm .06$ ($2.53 \pm .07$)	$1.78 \pm .05$ ($3.18 \pm .06$)	$2.08 \pm .07$ ($3.91 \pm .09$)
60°-70°	$1.53 \pm .05$ ($2.58 \pm .05$)	$1.83 \pm .05$ ($3.18 \pm .06$)	$2.30 \pm .09$ ($4.13 \pm .12$)
70°-90°	$1.43 \pm .08$ ($2.43 \pm .10$)	$1.73 \pm .09$ ($2.85 \pm .12$)	$2.33 \pm .20$ ($3.78 \pm .28$)
Average	$1.53 \pm .26$ ($2.64 \pm .29$)	$1.86 \pm .22$ ($3.19 \pm .28$)	$2.30 \pm .39$ ($4.19 \pm .51$)

in the top panel of Fig. 3, and fit each set of data with a linear curve using least squares analysis. In all wind channels, we find a subtle trend that the correlation length decreases as θ increases - the slopes of slow and medium winds are negative with a 2σ confidence, while the trend is less pronounced for fast wind, as shown in the legend of Fig. 3. This indicates that the longest average correlation lengths occur in the angular channel with the mean magnetic field direction quasi-aligned with the particle flow direction.

We also list, in parentheses in Table 2, the spatial lag where the correlation decreases by a factor of $1/2e$, denoted as $\lambda_{1/2e}$. The corresponding plot is shown in the bottom panel of Fig. 3. We find that $\lambda_{1/2e}$ decreases more noticeably as θ increases, suggesting that the observed correlation persists to larger distances in the parallel directions. Equivalently, the gradients at the

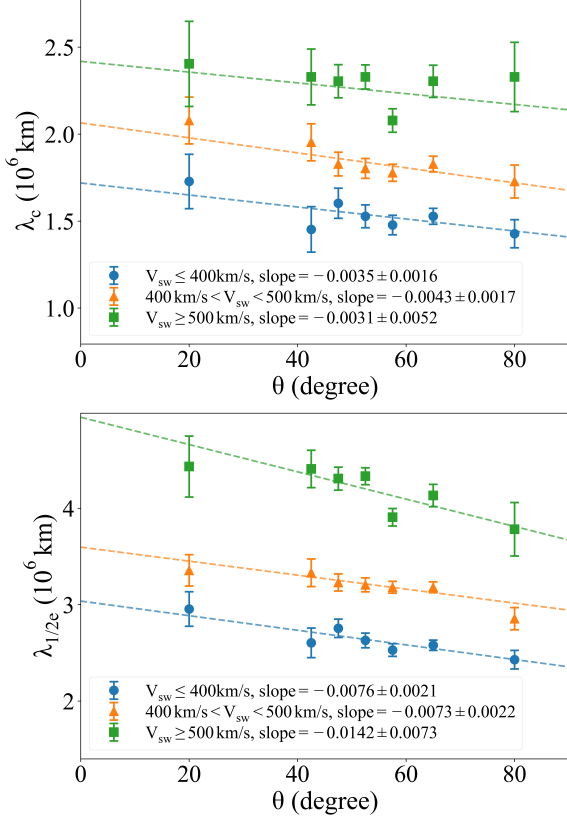


Figure 3. The correlation length λ_c (top panel) and the length $\lambda_{1/2e}$ where the correlation decreases by a factor of $1/2e$ (bottom panel) as functions of angular channel for slow, medium, and fast winds. The data and uncertainties are consistent with those listed in Table 2. Dashed lines show linear best fits with corresponding slopes listed in the legends.

outer scale of turbulence are moderately stronger in the perpendicular directions. Additionally, we observe that the correlation lengths are systematically longer in fast wind compared to slow wind. This latter difference appears to be clearer in density correlations compared with magnetic correlations (Weygand et al. 2011).

To better visualize the density correlation anisotropy for slow, medium, and fast winds, in Fig. 4 we plot the contour levels of the averaged autocorrelations $\hat{R}(\lambda)$ in perpendicular and parallel lag spaces through the transformation ($\lambda_{\perp} =$

$\lambda \sin \theta$, $\lambda_{\parallel} = \lambda \cos \theta$), following Dasso et al. (2005). The contours are computed in the first quadrant, then mirrored about the $\theta = 0^\circ$ and 90° axes under symmetry assumptions. This is a statistical demonstration of the Maltese cross geometry in density fluctuation fields.

It is evident that the outermost contours of constant correlation in Fig. 4, those with the smallest correlation values, are slightly elongated in the parallel direction for all three classes of wind speed. The effect is actually rather subtle for all wind channels. These contours of very low correlation values (the largest “circles”) may be characterized as weakly “2D-like” in the sense described in Dasso et al. (2005). However, the higher correlation contours (the smaller circles) tend to exhibit the opposite type of anisotropy that may be described as “slab-like”. Specifically, the $\hat{R} = 0.5$ contour for fast wind is somewhat “slab-like” with elongation in the perpendicular direction, and this tendency becomes more pronounced at the highest correlation values, as depicted in the bottom panel of Fig. 4. Meanwhile, the $\hat{R} = 0.5$ contours for slow and intermediate winds remain slightly 2D-like, even though they also become slab-like at the highest correlation values. This general tendency of the correlation contours and its dependence on wind speed is qualitatively consistent with the result from Dasso et al. (2005) for the magnetic field correlations, a comparison that we discuss in greater detail later.

The general increase in correlation lengths with increasing wind speed is also readily apparent in Fig. 4, where isocontours “expand” from the top to the bottom panel.

The above description of density anisotropies is quantified in Table 3. Here, we list the values for λ_{\perp} , λ_{\parallel} , and $\lambda_{\perp}/\lambda_{\parallel}$ in all three wind channels corresponding the following normalized correlations: $\hat{R} = 0.9, 0.7, 0.5, 1/e, 0.3, 1/2e$, and 0.1 . Scales larger than the correlation scale are considered the energy-containing scale, while smaller scales belong to the inertial range. The lags are calcu-

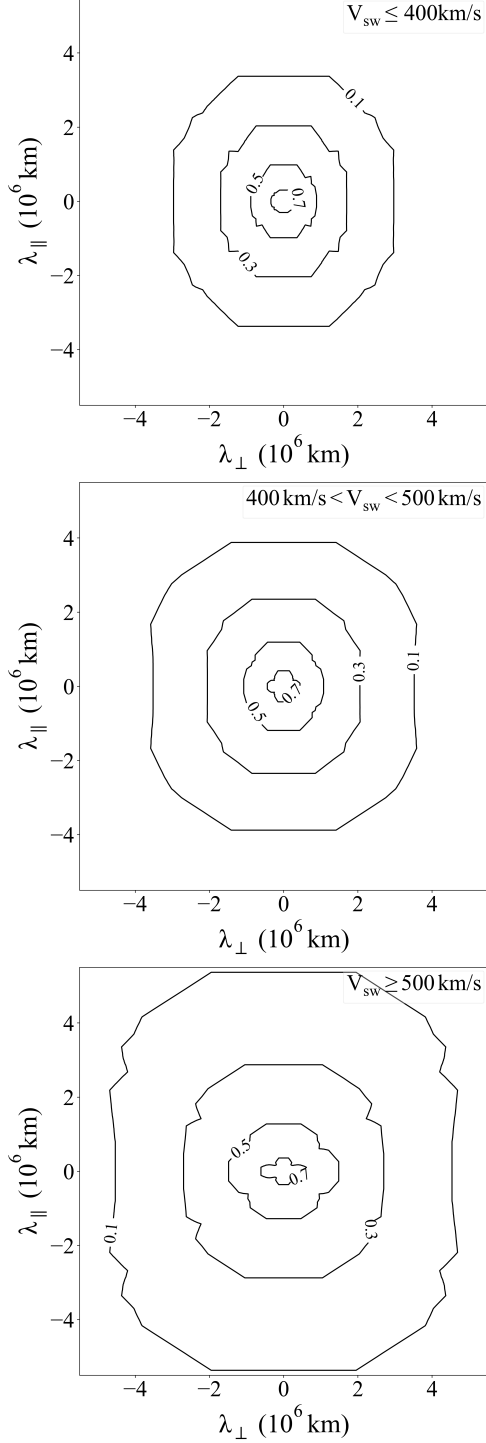


Figure 4. The correlation contours for slow (top panel), medium (middle panel), and fast (bottom panel) winds, calculated from Fig. 2 through the transformation ($\lambda_{\perp} = \lambda \sin \theta$, $\lambda_{\parallel} = \lambda \cos \theta$).

Table 3. Estimates of λ_{\perp} and λ_{\parallel} in units of 10^6 km as well as their ratio on the correlation contours $\hat{R}(\lambda) = 0.9, 0.7, 0.5, 1/e, 0.3, 1/2e$, and 0.1 for slow, medium, and fast winds.

	\hat{R}	λ_{\perp}	λ_{\parallel}	$\lambda_{\perp}/\lambda_{\parallel}$
≤ 400 km/s	0.9	0.05	0.03	1.78
	0.7	0.34	0.30	1.14
	0.5	0.89	0.98	0.90
	$1/e$	1.39	1.61	0.86
	0.3	1.70	2.03	0.84
	$1/2e$	2.37	2.77	0.85
	0.1	2.97	3.37	0.88
400-500 km/s	0.9	0.07	0.04	1.54
	0.7	0.44	0.42	1.05
	0.5	1.08	1.19	0.90
	$1/e$	1.68	1.93	0.87
	0.3	2.06	2.35	0.88
	$1/2e$	2.79	3.14	0.89
	0.1	3.52	3.88	0.91
≥ 500 km/s	0.9	0.13	0.04	3.31
	0.7	0.61	0.36	1.71
	0.5	1.48	1.28	1.16
	$1/e$	2.28	2.26	1.01
	0.3	2.70	2.87	0.94
	$1/2e$	3.71	4.16	0.89
	0.1	4.54	5.37	0.85

lated from Fig. 2 using $\lambda_{\perp} = \lambda(\hat{R}_{70^{\circ}-90^{\circ}}) \sin 80^{\circ}$ and $\lambda_{\parallel} = \lambda(\hat{R}_{0^{\circ}-40^{\circ}}) \cos 20^{\circ}$, or can be directly observed in Fig. 4. Note that due to the coarse binning at low θ , λ_{\parallel} may be underestimated and $\lambda_{\perp}/\lambda_{\parallel}$ may be overestimated. Fig. 5 shows how $\lambda_{\perp}/\lambda_{\parallel}$ varies with \hat{R} . We again observe that the correlations are slightly elongated along the parallel direction at small \hat{R} (large spatial lags), while for small spatial lags (large \hat{R}), corresponding to the inertial range, the correlations are elongated in the perpendicular direction.

5. DISCUSSION

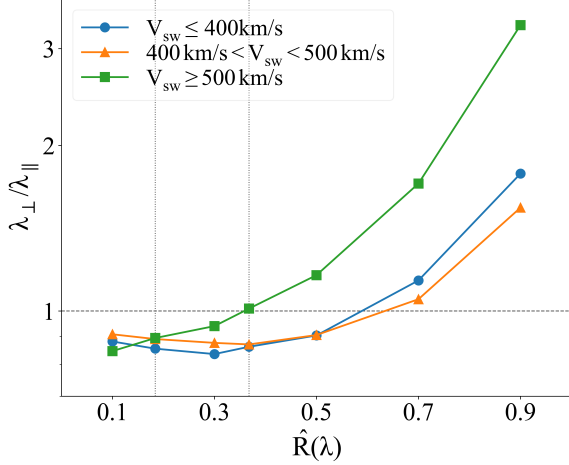


Figure 5. Estimates of $\lambda_{\perp}/\lambda_{\parallel}$ as functions of $\hat{R}(\lambda)$ for slow, medium, and fast winds. Dotted vertical lines indicate the $1/e$ and $1/2e$ correlation levels. Dashed horizontal line indicates where $\lambda_{\perp}/\lambda_{\parallel} = 1$.

There is a general tendency for MHD, and plasma turbulence in the MHD range of scales as well, to exhibit correlation anisotropy, and equivalently, spectral anisotropy relative to the direction of a regional mean magnetic field of sufficient strength (Shebalin et al. 1983; Oughton et al. 1994). Other effects may also introduce anisotropies by imposing preferred directions that influence regional and local dynamics. For example, in a structured and expanding medium such as the solar wind, large-scale plasma flows may introduce preferred directions that influence anisotropy. A notable effect is that of expansion, which, in the simplest case, selects the radial direction as preferred. Other relevant effects include regions of shear and compression occurring between high- and low-speed streams and near shocks, as well as interactions involving structures such as coronal mass ejections. One may expect that these various influences on anisotropy may operate at different length scales, and may have varying levels of influence on different physical quantities. For mostly practical reasons, solar wind studies on turbulence anisotropy have often concentrated on the magnetic field. The present report extends

this discussion to include the fluctuations in density.

More specifically, most previous examinations of anisotropy have considered the relatively local effects of the magnetic field direction on the rotational symmetry of magnetic fluctuations (Bieber et al. 1994, 1996). Based on results from laboratory experiments (Robinson & Rusbridge 1971) and numerical simulations (Shebalin et al. 1983; Oughton et al. 1994), the expectation is that MHD-scale turbulence will display a quasi-2D anisotropy relative to the field direction. This expectation, mainly based on theoretical examinations of incompressible dynamics, is reasonably well-confirmed in most analyses of solar wind rotational symmetry (Bieber et al. 1994, 1996). An exception is the study of Saur & Bieber (1999), which finds some support for a preferred role of the radial direction at relatively lower frequencies. The later finding suggests the influence of expansion, an effect clearly seen in WKB treatments (e.g. Völk & Aplers 1973).

Considering a broader context, the dynamics in the solar wind at 1 au may consist of an admixture of incompressible and compressible parts. In this more realistic portrayal, more complex influences on rotational symmetry may be anticipated. In particular, the incompressible tendency towards a quasi-2D configuration merges with the relatively isotropic spectral (and correlation) statistics attributed to the compressible dynamics. Indeed, compressible MHD simulations (Matthaeus et al. 1996; Du et al. 2023) with Mach number, plasma β , and $\delta B/B$ similar to those of the solar wind indicate that density spectra are anisotropic, but less so than the anisotropy seen in incompressible simulations (Oughton et al. 1994). This appears to be consistent with the current findings, wherein the correlation lengths parallel and perpendicular to the mean magnetic field differ from one another by only a small relative fraction. The present finding also suggests a more complex scenario in which the sense of anisotropy varies across scales.

It has been previously suggested (Dasso et al. 2005; Weygand et al. 2011) that for the magnetic field in the solar wind, the parallel correlation scale is larger than the perpendicular correlation scale by a factor of around 2 for the slow solar wind. This is a modest 2D-like anisotropy compared to what is expected at smaller scales in the inertial range. However, such a ratio is considerably larger than that of the density correlation scales reported here.

Here, for density fluctuations, the sense of anisotropy at the correlation scale, whether measured at the $1/e$ or the $1/2e$ level, is mainly of the “2D” type. (The fast wind is essentially isotropic at the $1/e$ scale but becomes 2D at larger scales.) We suggest that the weaker outer-scale anisotropy of the density is due to the effects of the admixture of more anisotropic incompressible turbulence with less anisotropic compressible turbulence, consistent with previous numerical results (see, e.g., Fig. 5 of Matthaeus et al. 1996).

It is interesting, perhaps a bit surprising and of potential significance, that at smaller scales (higher correlation values), the sense of density anisotropy reverses and favors slab-like symmetries. This trend occurs in all wind speed channels and is especially dramatic for fast wind. This is reminiscent of the sense of magnetic anisotropy at correlation scales in fast wind (Dasso et al. 2005). Furthermore, by inspection of the magnetic correlation contours in Dasso et al. (2005), it appears that slab-like symmetry occurs across a wide range of scales in fast wind. This however was not quantified. But for slow wind, the 2D-like sense of magnetic anisotropy mentioned above as present at the correlation scale remains (as seen by inspection) 2D-like over a reasonably wide range of scales. Furthermore, in the above-quoted compressible MHD simulation results (Matthaeus et al. 1996), the inertial range contours of density spectra appear to be of the 2D type, although not dramatically so. Finally, we note that our finding of slab-like density in the fast wind inertial range

also seems to contradict Fig. 5 and 6 of Chen et al. (2012), who use Ulysses data and adopt $|\mathbf{B}|$ as a proxy for compressive fluctuations. A major difference, however, is that the analysis of Chen et al. (2012) is carried out in a coordinate system based on a local definition of the mean field. Such a procedure systematically increases the ratio of perpendicular to parallel structure functions, thus favoring 2D-like interpretations (Matthaeus et al. 2012). Our computation of mean fields integrated over longer times is chosen to avoid this bias.

We cannot rule out the appearance of field aligned (2D-like) anisotropies at much smaller scales, possibly for all wind speeds. Indeed, these are favored by coronal observations such as Armstrong et al. (1990). The study found field-aligned elongated structures having anisotropy ratios that increase with increasing heliocentric distance from 2 to about 10 solar radii. However, these observations were at much smaller scales, and much closer to the sun, relative to the present large-scale observations at 1 au. Nevertheless, these authors did suggest that solar wind density anisotropy varies with scale.

The present results for the anisotropy of density stand in substantial contrast to expectations based on magnetic and velocity field spectra in incompressible simulations and in solar wind observations. The basis of this expectation is that the incompressible cascade, which presumably is a major factor in the solar wind dynamics, is well known to favor 2D-like anisotropies (Oughton et al. 2015). The reasons for this departure remain unclear at present, but most likely pertain to the way compressible fluctuations are generated in the solar wind. Further research will be required to arrive at a clearer understanding.

Future observations from the PUNCH mission (Deforest et al. 2022) will provide us with solar wind density data in regions of the inner heliosphere yet unexplored and with an unprecedented field of view. As observed in DeForest et al. (2016), the solar wind shows a transition from

“striated” to “focculated” features, suggesting an evolution toward isotropization (Cuesta et al. 2022). Using the white-light images obtained from PUNCH, it will be possible to recover unprecedented mapping of solar wind density. Such measurements will be used to perform analyses similar to those presented in this paper, that will provide invaluable knowledge about the radial evolution of solar wind anisotropy.

The velocity and density data were downloaded from https://spdf.gsfc.nasa.gov/pub/data/ace/swepam/level2_hdf/ions_64sec. This research is partially supported by the NASA LWS grant 80NSSC20K0377 (subcontract 655-001), and by the NASA IMAP project at UD under subcontract SUB0000317 from Princeton University. R.C. and M.E.C. acknowledge LANL’s hospitality during Summer 2022, when part of this work was performed.

APPENDIX

The separation of data intervals into three wind speed classes is a central part of this analysis. To ensure a reasonable level of statistical validity in each class, we base the partitioning by speed on an understanding of its probability distribution, as shown in Fig. 6. The boundaries for slow, medium, and fast wind channels are represented by dotted vertical lines to show an almost equal number of counts in each channel.

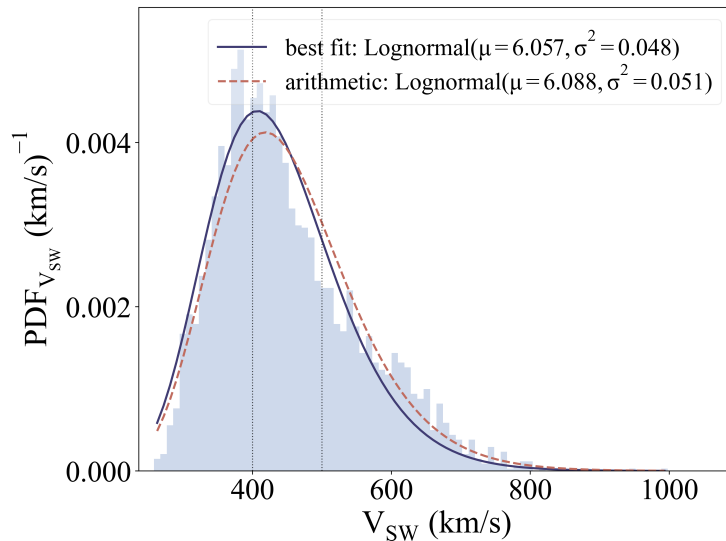


Figure 6. Shaded histogram shows the distribution of solar wind speeds. Dotted vertical lines represent the boundaries of the solar wind speed channels. Solid curve shows the best-fit lognormal distribution. Dashed curve shows the lognormal distribution derived from the arithmetic mean and variance of the wind speed samples. Parameters of both lognormal distributions are listed in the legend.

REFERENCES

- Adhikari, L., Zank, G. P., Hunana, P., et al. 2017, *ApJ*, 841, 85, doi: [10.3847/1538-4357/aa6f5d](https://doi.org/10.3847/1538-4357/aa6f5d)
- Armstrong, J. W., Coles, W. A., Kojima, M., & Rickett, B. J. 1990, *ApJ*, 358, 685, doi: [10.1086/169022](https://doi.org/10.1086/169022)
- Balmaceda, L. A., Solanki, S. K., Krivova, N. A., & Foster, S. 2009, *Journal of Geophysical Research (Space Physics)*, 114, A07104, doi: [10.1029/2009JA014299](https://doi.org/10.1029/2009JA014299)
- Barnes, A. 1981, *J. Geophys. Res.*, 86, 7498, doi: [10.1029/JA086iA09p07498](https://doi.org/10.1029/JA086iA09p07498)
- Barnes, A., & Hollweg, J. V. 1974, *J. Geophys. Res.*, 79, 2302, doi: [10.1029/JA079i016p02302](https://doi.org/10.1029/JA079i016p02302)
- Batchelor, G. K. 1970, *The Theory of Homogeneous Turbulence* (Cambridge, UK: Cambridge University Press)
- Bellamy, B. R., Cairns, I. H., & Smith, C. W. 2005, *J. Geophys. Res.*, 110, A10104, doi: [10.1029/2004JA010952](https://doi.org/10.1029/2004JA010952)
- Bieber, J. W., Matthaeus, W. H., Smith, C. W., et al. 1994, *ApJ*, 420, 294, doi: [10.1086/173559](https://doi.org/10.1086/173559)
- Bieber, J. W., Wanner, W., & Matthaeus, W. H. 1996, *J. Geophys. Res.*, 101, 2511, doi: [10.1029/95JA02588](https://doi.org/10.1029/95JA02588)
- Blackman, R. B., & Tukey, J. W. 1958, *The Measurement of Power Spectra* (Dover)
- Borovsky, J. E. 2012, *Journal of Geophysical Research (Space Physics)*, 117, A05104, doi: [10.1029/2011JA017499](https://doi.org/10.1029/2011JA017499)
- Bruno, R., & Carbone, V. 2013, *Living Reviews in Solar Physics*, 10, 2, doi: [10.12942/lrsp-2013-2](https://doi.org/10.12942/lrsp-2013-2)
- Celnikier, L. M., Muschietti, L., & Goldman, M. V. 1987, *A&A*, 181, 138
- Chandran, B. D. G. 2005, *PhRvL*, 95, 265004, doi: [10.1103/PhysRevLett.95.265004](https://doi.org/10.1103/PhysRevLett.95.265004)
- Chandran, B. D. G., & Backer, D. C. 2002, *ApJ*, 576, 176, doi: [10.1086/340792](https://doi.org/10.1086/340792)
- Chen, C. H. K., Mallet, A., Schekochihin, A. A., et al. 2012, *ApJ*, 758, 120, doi: [10.1088/0004-637X/758/2/120](https://doi.org/10.1088/0004-637X/758/2/120)
- Chen, C. H. K., Mallet, A., Yousef, T. A., Schekochihin, A. A., & Horbury, T. S. 2011, *MNRAS*, 415, 3219, doi: [10.1111/j.1365-2966.2011.18933.x](https://doi.org/10.1111/j.1365-2966.2011.18933.x)
- Cho, J., & Lazarian, A. 2002, *PhRvL*, 88, 245001, doi: [10.1103/PhysRevLett.88.245001](https://doi.org/10.1103/PhysRevLett.88.245001)
- Cho, J., Lazarian, A., & Vishniac, E. T. 2002, *ApJ*, 564, 291, doi: [10.1086/324186](https://doi.org/10.1086/324186)
- Coles, W. A., & Harmon, J. K. 1989, *ApJ*, 337, 1023, doi: [10.1086/167173](https://doi.org/10.1086/167173)
- Cuesta, M. E., Chhiber, R., Roy, S., et al. 2022, *ApJL*, 932, L11, doi: [10.3847/2041-8213/ac73fd](https://doi.org/10.3847/2041-8213/ac73fd)
- Dasso, S., Milano, L. J., Matthaeus, W. H., & Smith, C. W. 2005, *ApJL*, 635, L181, doi: [10.1086/499559](https://doi.org/10.1086/499559)
- Deforest, C., Killough, R., Gibson, S., et al. 2022, in *2022 IEEE Aerospace Conference*, 1–11, doi: [10.1109/AERO53065.2022.9843340](https://doi.org/10.1109/AERO53065.2022.9843340)
- DeForest, C. E., Matthaeus, W. H., Viall, N. M., & Cranmer, S. R. 2016, *ApJ*, 828, 66, doi: [10.3847/0004-637X/828/2/66](https://doi.org/10.3847/0004-637X/828/2/66)
- Du, S., Li, H., Gan, Z., & Fu, X. 2023, *ApJ*, 946, 74, doi: [10.3847/1538-4357/acc10b](https://doi.org/10.3847/1538-4357/acc10b)
- Frisch, U. 1995, *Turbulence: the legacy of AN Kolmogorov* (Cambridge university press)
- Gan, Z., Li, H., Fu, X., & Du, S. 2022, *ApJ*, 926, 222, doi: [10.3847/1538-4357/ac4d9d](https://doi.org/10.3847/1538-4357/ac4d9d)
- Germano, M. 1992, *Journal of Fluid Mechanics*, 238, 325, doi: [10.1017/S0022112092001733](https://doi.org/10.1017/S0022112092001733)
- Goldreich, P., & Sridhar, S. 1995, *ApJ*, 438, 763, doi: [10.1086/175121](https://doi.org/10.1086/175121)
- Hamilton, K., Smith, C. W., Vasquez, B. J., & Leamon, R. J. 2008, *Journal of Geophysical Research (Space Physics)*, 113, A01106, doi: [10.1029/2007JA012559](https://doi.org/10.1029/2007JA012559)
- Horbury, T. S., Wicks, R. T., & Chen, C. H. K. 2012, *SSRv*, 172, 325, doi: [10.1007/s11214-011-9821-9](https://doi.org/10.1007/s11214-011-9821-9)
- Kellogg, P. J., & Horbury, T. S. 2005, *Annales Geophysicae*, 23, 3765, doi: [10.5194/angeo-23-3765-2005](https://doi.org/10.5194/angeo-23-3765-2005)
- Kontar, E. P., Emslie, A. G., Clarkson, D. L., et al. 2023, *ApJ*, 956, 112, doi: [10.3847/1538-4357/acf6c1](https://doi.org/10.3847/1538-4357/acf6c1)

- Malaspina, D. M., Kellogg, P. J., Bale, S. D., & Ergun, R. E. 2010, *ApJ*, 711, 322, doi: [10.1088/0004-637X/711/1/322](https://doi.org/10.1088/0004-637X/711/1/322)
- Matthaeus, W. H., Ghosh, S., Oughton, S., & Roberts, D. A. 1996, *J. Geophys. Res.*, 101, 7619, doi: [10.1029/95JA03830](https://doi.org/10.1029/95JA03830)
- Matthaeus, W. H., & Goldstein, M. L. 1982, *J. Geophys. Res.*, 87, 6011, doi: [10.1029/JA087iA08p06011](https://doi.org/10.1029/JA087iA08p06011)
- Matthaeus, W. H., Goldstein, M. L., & Roberts, D. A. 1990, *J. Geophys. Res.*, 95, 20673, doi: [10.1029/JA095iA12p20673](https://doi.org/10.1029/JA095iA12p20673)
- Matthaeus, W. H., Servidio, S., Dmitruk, P., et al. 2012, *ApJ*, 750, 103, doi: [10.1088/0004-637X/750/2/103](https://doi.org/10.1088/0004-637X/750/2/103)
- McComas, D. J., Bame, S. J., Barker, P., et al. 1998, *SSRv*, 86, 563, doi: [10.1023/A:1005040232597](https://doi.org/10.1023/A:1005040232597)
- McComas, D. J., Barraclough, B. L., Funsten, H. O., et al. 2000, *J. Geophys. Res.*, 105, 10419, doi: [10.1029/1999JA000383](https://doi.org/10.1029/1999JA000383)
- Narita, Y., Glassmeier, K. H., Sahraoui, F., & Goldstein, M. L. 2010, *PhRvL*, 104, 171101, doi: [10.1103/PhysRevLett.104.171101](https://doi.org/10.1103/PhysRevLett.104.171101)
- Oughton, S., & Matthaeus, W. H. 2020, *ApJ*, 897, 37, doi: [10.3847/1538-4357/ab8f2a](https://doi.org/10.3847/1538-4357/ab8f2a)
- Oughton, S., Matthaeus, W. H., Wan, M., & Osman, K. T. 2015, *Philosophical Transactions of the Royal Society of London Series A*, 373, 20140152, doi: [10.1098/rsta.2014.0152](https://doi.org/10.1098/rsta.2014.0152)
- Oughton, S., Priest, E. R., & Matthaeus, W. H. 1994, *Journal of Fluid Mechanics*, 280, 95, doi: [10.1017/S0022112094002867](https://doi.org/10.1017/S0022112094002867)
- Panchev, S. 1971, *Random Functions and Turbulence* (New York: Pergamon Press)
- Robinson, D. C., & Rusbridge, M. G. 1971, *Physics of Fluids*, 14, 2499, doi: [10.1063/1.1693359](https://doi.org/10.1063/1.1693359)
- Roy, S., Chhiber, R., Dasso, S., Ruiz, M. E., & Matthaeus, W. H. 2021, *ApJL*, 919, L27, doi: [10.3847/2041-8213/ac21d2](https://doi.org/10.3847/2041-8213/ac21d2)
- Saur, J., & Bieber, J. W. 1999, *J. Geophys. Res.*, 104, 9975, doi: [10.1029/1998JA900077](https://doi.org/10.1029/1998JA900077)
- Shaikh, D., & Zank, G. P. 2010, *MNRAS*, 402, 362, doi: [10.1111/j.1365-2966.2009.15881.x](https://doi.org/10.1111/j.1365-2966.2009.15881.x)
- Shalchi, A. 2009, *Nonlinear Cosmic Ray Diffusion Theories*, Vol. 362, doi: [10.1007/978-3-642-00309-7](https://doi.org/10.1007/978-3-642-00309-7)
- Shebalin, J. V., Matthaeus, W. H., & Montgomery, D. 1983, *Journal of Plasma Physics*, 29, 525, doi: [10.1017/S0022377800000933](https://doi.org/10.1017/S0022377800000933)
- Smith, C. W., L'Heureux, J., Ness, N. F., et al. 1998, *SSRv*, 86, 613, doi: [10.1023/A:1005092216668](https://doi.org/10.1023/A:1005092216668)
- Taylor, G. I. 1938, *Proceedings of the Royal Society of London Series A*, 164, 476, doi: [10.1098/rspa.1938.0032](https://doi.org/10.1098/rspa.1938.0032)
- Usmanov, A. V., Matthaeus, W. H., Goldstein, M. L., & Chhiber, R. 2018, *ApJ*, 865, 25, doi: [10.3847/1538-4357/aad687](https://doi.org/10.3847/1538-4357/aad687)
- Völk, H. J., & Aplers, W. 1973, *Ap&SS*, 20, 267, doi: [10.1007/BF00642204](https://doi.org/10.1007/BF00642204)
- Weygand, J. M., Matthaeus, W. H., Dasso, S., & Kivelson, M. G. 2011, *Journal of Geophysical Research (Space Physics)*, 116, A08102, doi: [10.1029/2011JA016621](https://doi.org/10.1029/2011JA016621)
- Zank, G. P., Jetha, N., Hu, Q., & Hunana, P. 2012, *ApJ*, 756, 21, doi: [10.1088/0004-637X/756/1/21](https://doi.org/10.1088/0004-637X/756/1/21)
- Zank, G. P., Zhao, L. L., Adhikari, L., et al. 2023, *ApJS*, 268, 18, doi: [10.3847/1538-4365/acdf5d](https://doi.org/10.3847/1538-4365/acdf5d)